Electron energy loss spectroscopy simulation by a frequency domain surface integral equation solver

İsmail Enes UYSAL[1,2,*]
[1]Department of Electrical and Electronics Engineering, Faculty of Engineering and Architecture,
İstanbul Gelişim University, İstanbul, Turkey
[2]Elements Strategy Initiative Center for Magnetic Materials, National Institute for Materials Science, Tsukuba,
Ibaraki, Japan

Abstract: Plasmonic nanoparticles have been mostly studied using conventional light sources. Recently, electron energy loss spectroscopy (EELS) has started to be used to analyze plasmonic nanoparticles where incident electromagnetic fields are created by swift electrons. To accurately simulate EELS experiments, several numerical methods have been adapted. In this paper, a frequency domain surface integral equation (FDSIE) solver is modified to simulate EELS for plasmonic nanoparticles of gold and silver. Accuracy and versatility of the proposed FDSIE solver are shown by several numerical examples and compared to existing numerical, analytical, and experimental results.

Key words: Electron energy loss spectroscopy, surface integral equation, method of moments

1. Introduction

The collective oscillations of electrons of nanoparticles (NPs) give rise to plasmon resonances. Manipulation of plasmon resonances are crucial for various applications such as bio-imaging, bio-medicine, and improvement of solar cells [1]. Plasmonic behavior of NPs have been examined mostly using conventional light sources such as lasers and fluorescent lamps. Recently, electron energy loss spectroscopy (EELS) experiments have been performed to analyze plasmonic behavior of NPs thanks to the high spatial and energy resolution of EELS [2, 3].

Two major differences between conventional light scattering experiments and EELS are the incident electromagnetic field and the collected data after scattering. In the former, most of the time, the incident field is assumed to be a plane electromagnetic wave propagating in a given direction with a fixed polarization. Then the scattered light is measured at a certain angle or collected by an integrating sphere. However, in EELS, incident fields are created by a beam of electron and the measurement is on the energy loss of the electron. Energy loss of the electron depends on the materials along or near the electron path. When the electron passes through materials, energy loss spectra give signatures about their atomic structure. When the electron passes nearby an NP, it creates a field which excites the NP. The scattered light reaches back to the electron beam causing an energy loss. The resonances of the EELS spectra correspond to the plasmon resonances of the NP. Due to the excitation of the electron beam, new plasmon resonances of NP could be studied in EELS. These resonances are not seen in conventional plasmonic experiments where incident light is a plane wave [4].

In accordance with the shift in the experimental approach, several numerical methods, such as boundary

---

*Correspondence: uysal.ismailenes@nims.go.jp

element method (BEM) [5, 6], frequency domain surface integral equation (FDSIE) [7], finite difference time domain (FDTD) [8], and discrete dipole approximation (DDA) [9], were modified to simulate EELS experiments. In this paper, another FDSIE solver is adapted for the simulation of EELS experiment.

FDTD and DDA are usually preferred solvers due to their simple implementation and easy use. However, these solvers require volumetric discretization of NPs leading to higher number of unknowns. Specifically, on the boundaries of NPs, electromagnetic fields change rapidly and therefore have to be modeled by finer meshes. Moreover, artificial boundary conditions in FDTD might render the simulations inaccurate [10]. To avoid these drawbacks, FDSIE (or BEM) could be employed because it requires discretization of surfaces leading to a smaller number of unknowns and it satisfies radiation condition implicitly without requiring artificial boundary conditions.

BEM and FDSIE are essentially same solvers based on the surface equivalence principle and the discretization of surfaces of NPs. The main difference is in the implementation of the solvers. In BEM [6], surfaces are meshed by triangular patches; unknowns are electric charges and electric current densities; electric scalar and vector potential is used to construct the equation; more importantly, a point collocation method is employed. Here, surfaces are meshed by triangular patches; unknowns are electric and magnetic current densities; electric and magnetic fields are used to construct the main equation; lastly, well-known Rao–Wilton–Glisson (RWG) basis functions [11] used with Galerkin testing. Although there are few differences, the main difference is in the basis functions and testing; hence, BEM [6] could be named as point collocation FDSIE. However, here, the method in [6] is referred to as BEM to be consistent with the literature [2, 5, 6, 12].

In terms of EELS simulations, there are subtle differences between the existing FDSIE (or BEM) solvers and the present solver. Electron energy loss probability is defined as a line integral and could be computed along the path of the electron [2, 8]. However, in [6], the computation of the line integral is reduced to an integral on the surface of the NP. Although this is numerically feasible and correct, it hinders the comprehension of physical aspect of the experiment. In [7], electron energy loss is related to the scattering cross section and absorption cross section of the NP. However, scattering cross section is computed by the far fields while EELS is a near-field phenomena. Here, energy loss probability is explicitly computed along the path of the electron, as explained in the formulations, such that it gives a physical insight to the mechanism of EELS.

In the next section, EELS theory is given and FDSIE formulation is detailed. Then, numerical results are presented to verify the accuracy and the versatility of the proposed solver. Finally, in the last section, conclusions are drawn.

2. Method

In this section, a brief theory of EELS and a formulation of FDSIE is given. Among various FDSIE formulations, Poggio–Miller–Chan–Harrington–Wu–Tsai (PMCHWT) [13] is chosen because it gives accurate results for plasmonic NPs [14]. Note that the present formulation of FDSIE is not specific to EELS simulation. The main difference is two-fold. First, the incident fields are created by swift electrons in EELS. Second, the computation of the energy loss function is carried out by using scattered near fields.

2.1. EELS theory

Consider an electron moving with a constant speed (v) comparable to the speed of light (c) in a medium that has the permittivity (ε_0) and the permeability (μ_0). It is assumed that, without loss of generality, the electron

moves along the z-axis passing through the origin. The motion of the electron gives rise to the incident fields [2]

$$\boldsymbol{E}_0^{\mathrm{inc}}(\boldsymbol{r}) = -\frac{q_e \omega e^{-j\omega z/v}}{2\pi v^2 \varepsilon_0 \gamma} \left[\frac{j}{\gamma} K_0 \left(\frac{\rho \omega}{v\gamma} \right) \hat{\boldsymbol{z}} + K_1 \left(\frac{\rho \omega}{v\gamma} \right) \hat{\boldsymbol{\rho}} \right], \tag{1}$$

$$\boldsymbol{H}_0^{\mathrm{inc}}(\boldsymbol{r}) = -\frac{q_e \omega e^{-j\omega z/v}}{2\pi v \gamma} K_1 \left(\frac{\rho \omega}{v\gamma} \right) \hat{\boldsymbol{\phi}}.$$

Here, q_e is the charge of the electron, $\gamma = (1 - v^2/c^2)^{-1/2}$ is the Lorentz contraction factor, K_0 and K_1 are modified Bessel functions, ω is the angular frequency, $\rho = \sqrt{x^2 + y^2}$ is the radial distance from the z-axis, and $(\hat{\boldsymbol{z}}, \hat{\boldsymbol{\rho}}, \hat{\boldsymbol{\phi}})$ are the unit vectors in cylindrical coordinates. Time dependence of the fields are assumed to be $e^{j\omega t}$ and SI units are used unlike [2].

Due to the presence of NP, scattered fields occur and act back to the electron. The energy loss of the electron caused by scattered fields could be written as:

$$\Delta E = q_e \int \boldsymbol{v} \cdot \boldsymbol{E}_0^{\mathrm{sca}}(\boldsymbol{r_e}(t), t) dt = \int_0^\infty \hbar \omega \Gamma(\omega) d\omega. \tag{2}$$

Here, $\boldsymbol{r_e}(t)$ is the path of the electron, $\boldsymbol{E}_0^{\mathrm{sca}}(\boldsymbol{r_e}(t), t)$ is the scattered electric field in time domain, $\hbar$ is the reduced Planck's constant, and $\Gamma(\omega)$ is the loss probability function. It is assumed that the speed of the electron is constant, i.e. no-recoil approximation. This approximation is valid when the electron has a high speed [2]. Using Fourier transform, energy loss probability could be written as in [5]:

$$\Gamma(\omega) = \frac{q_e}{\pi \hbar \omega} \int Re\{e^{j\omega t} \boldsymbol{v} \cdot \boldsymbol{E}_0^{\mathrm{sca}}(\boldsymbol{r_e}(t), \omega)\} dt = \frac{q_e}{\pi \hbar \omega} \int Re\{e^{j\omega z/v} \hat{\boldsymbol{z}} \cdot \boldsymbol{E}_0^{\mathrm{sca}}(z, \omega)\} dz. \tag{3}$$

Hence, the loss probability computed as a line integral of $\boldsymbol{E}_0^{\mathrm{sca}}(z, \omega)$ that is the scattered electric field in frequency domain. Eq. (3) could be simply approximated by:

$$\Gamma(\omega) \approx \frac{q_e}{\pi \hbar \omega} \sum_{i=1}^{N_\Gamma} Re\{e^{\frac{j\omega z_i}{v}} \hat{\boldsymbol{z}} \cdot \boldsymbol{E}_0^{\mathrm{sca}}(z_i, \omega)\} \Delta z. \tag{4}$$

In Eq. (4), N_Γ is the number of integration points, $\Delta z = L/N_\Gamma$, where L is the length of the path of the electron, and $z_i = -L/2 + i\Delta z$. Theoretically, L should be infinite, but it will be shown that choosing L comparable to the size of the NP ensures the accuracy of the approximation. When the electron passes through a substrate, a bulk loss term which depends only on the thickness and permittivity of the substrate $\Gamma_{Bulk}(\omega)$ should be added to the $\Gamma(\omega)$ [2].

2.2. Formulation of FDSIE

This section describes the surface integral equation solver used for computing the fields scattered from an NP under excitation by an incident electromagnetic field. For the sake of simplicity, formulation is given for a single NP. Generalization of the formulation for multiple scattering objects could be found in [15]. Let V_1 represent the volume of an NP residing in an unbounded background medium denoted by V_0. Constant permittivity and permeability in V_i, $i \in \{0, 1\}$ are ε_i and μ_i, respectively. Let S denote the surface enclosing V_1. An electromagnetic wave with electric and magnetic fields, $\mathbf{E}_0^{\mathrm{inc}}(\boldsymbol{r})$ and $\boldsymbol{H}_0^{\mathrm{inc}}(\boldsymbol{r})$, excites the scatterer.

Enforcing the tangential continuity of the total electric and magnetic fields, $\boldsymbol{E}_i(\boldsymbol{r}) = \boldsymbol{E}_i^{\text{inc}}(\boldsymbol{r}) + \boldsymbol{E}_i^{\text{sca}}(\boldsymbol{r})$ and $\boldsymbol{H}_i(\boldsymbol{r}) = \boldsymbol{H}_i^{\text{inc}}(\boldsymbol{r}) + \boldsymbol{H}_i^{\text{sca}}(\boldsymbol{r})$, on S yields the PMCHWT surface integral equation [13]:

$$\widehat{\mathbf{n}}(\mathbf{r}) \times \mathbf{E}_0^{\text{inc}}(\mathbf{r}) = -\widehat{\mathbf{n}}(\mathbf{r}) \times [\mathbf{E}_1^{\text{sca}}(\mathbf{r}) - \mathbf{E}_0^{\text{sca}}(\mathbf{r})], \tag{5}$$

$$\widehat{\mathbf{n}}(\mathbf{r}) \times \mathbf{H}_0^{\text{inc}}(\mathbf{r}) = -\widehat{\mathbf{n}}(\mathbf{r}) \times [\mathbf{H}_1^{\text{sca}}(\mathbf{r}) - \mathbf{H}_0^{\text{sca}}(\mathbf{r})].$$

Here, $\widehat{\mathbf{n}}(\mathbf{r})$ is the unit normal vector at $\mathbf{r}$, $\mathbf{r} \in S$, pointing towards V_0, and $\mathbf{E}_i^{\text{sca}}(\mathbf{r})$ and $\mathbf{H}_i^{\text{sca}}(\mathbf{r})$ are the scattered electric and magnetic fields in V_i, $i \in \{0, 1\}$. One can introduce equivalent current densities $\mathbf{J}(\mathbf{r}) = -\widehat{\mathbf{n}}(\mathbf{r}) \times \mathbf{H}_1(\mathbf{r}) = \widehat{\mathbf{n}}(\mathbf{r}) \times \mathbf{H}_0(\mathbf{r})$ and $\mathbf{M}(\mathbf{r}) = \widehat{\mathbf{n}}(\mathbf{r}) \times \mathbf{E}_1(\mathbf{r}) = -\widehat{\mathbf{n}}(\mathbf{r}) \times \mathbf{E}_0(\mathbf{r})$ on S. Using the surface equivalence principle, $\mathbf{E}_i^{\text{sca}}(\mathbf{r})$ and $\mathbf{H}_i^{\text{sca}}(\mathbf{r})$ are expressed in terms of $\mathbf{J}(\mathbf{r})$ and $\mathbf{M}(\mathbf{r})$:

$$\mathbf{E}_0^{\text{sca}}(\mathbf{r}) = -\mathcal{L}_0\{\mathbf{J}(\mathbf{r})\} + \mathcal{K}_0\{\mathbf{M}(\mathbf{r})\}, \tag{6}$$

$$\mathbf{H}_0^{\text{sca}}(\mathbf{r}) = -\frac{\varepsilon_0}{\mu_0}\mathcal{L}_0\{\mathbf{M}(\mathbf{r})\} - \mathcal{K}_0\{\mathbf{J}(\mathbf{r})\},$$

$$\mathbf{E}_1^{\text{sca}}(\mathbf{r}) = \mathcal{L}_1\{\mathbf{J}(\mathbf{r})\} - \mathcal{K}_1\{\mathbf{M}(\mathbf{r})\}, \tag{7}$$

$$\mathbf{H}_1^{\text{sca}}(\mathbf{r}) = \frac{\varepsilon_1}{\mu_1}\mathcal{L}_1\{\mathbf{M}(\mathbf{r})\} + \mathcal{K}_1\{\mathbf{J}(\mathbf{r})\},$$

where the integral operators $\mathcal{L}_i\{.\}$ and $\mathcal{K}_i\{.\}$ are given by

$$\mathcal{L}_i\{\mathbf{X}(\mathbf{r})\} = \frac{j\omega\mu_i}{4\pi}\int_S \frac{\mathrm{e}^{-jk_iR}\mathbf{X}(\mathbf{r}')}{R}ds' - \frac{1}{j\omega4\pi\varepsilon_i}\nabla\int_S \frac{\mathrm{e}^{-jk_iR}\nabla'\cdot\mathbf{X}(\mathbf{r}')}{R}ds' \tag{8}$$

$$\mathcal{K}_i\{\mathbf{X}(\mathbf{r})\} = \frac{1}{4\pi}\int_S \mathbf{X}(\mathbf{r}') \times \nabla\frac{\mathrm{e}^{-jk_iR}}{R}ds', \tag{9}$$

$k_i = \omega\sqrt{\varepsilon_i(\omega)\mu_i}$ is the wavenumber in V_i, $\varepsilon_i(\omega)$ is the frequency-dependent permittivity, and $R = |\mathbf{r} - \mathbf{r}'|$ is the distance between observation and source point $\mathbf{r}$ and $\mathbf{r}'$ on S. To numerically solve Eq. (5), first S is discretized into triangular patches. Then the unknown current densities $\mathbf{J}(\mathbf{r})$ and $\mathbf{M}(\mathbf{r})$ are approximated using

$$\mathbf{J}(\mathbf{r}) = \sum_{l=1}^{N} J_l\mathbf{f}_l(\mathbf{r}), \tag{10}$$

$$\mathbf{M}(\mathbf{r}) = \sum_{l=1}^{N} M_l\mathbf{f}_l(\mathbf{r}).$$

Here, $\mathbf{f}_l(\mathbf{r})$ represent the RWG basis functions [11], each of which is defined over a pair of triangular patches that share an edge. N is the total number of RWGs defined on the discretized S. J_l and M_l are the unknown current coefficients to be solved for. Inserting Eq. (10) into Eq. (5) and Galerkin testing the resulting equation with $\mathbf{f}_m(\mathbf{r})$, $m = 1, ..., N$, yields the matrix system

$$\mathbf{ZI} = \mathbf{V}, \tag{11}$$

where the $2N \times 1$ vector $\mathbf{I} = [J_1, .., J_N, M_1, .., M_N]^T$ holds the unknown current coefficients, the entries of the $2N \times 1$ excitation vector are given by:

$$\mathbf{V}_m = \langle \mathbf{f}_m(\mathbf{r}), \widehat{\mathbf{n}}(\mathbf{r}) \times \mathbf{E}_0^{\mathrm{inc}}(\mathbf{r}) \rangle, \tag{12}$$

$$\mathbf{V}_{m+N} = \langle \mathbf{f}_m(\mathbf{r}), \widehat{\mathbf{n}}(\mathbf{r}) \times \mathbf{H}_0^{\mathrm{inc}}(\mathbf{r}) \rangle, m = 1, ..., N,$$

and the entries of the $2N \times 2N$ matrix $\mathbf{Z}$ are given by:

$$\mathbf{Z}_{m,l} = \langle \mathbf{f}_m(\mathbf{r}), \mathcal{L}_0\{\mathbf{f}_l(\mathbf{r})\} + \mathcal{L}_1\{\mathbf{f}_l(\mathbf{r})\} \rangle, \tag{13}$$

$$\mathbf{Z}_{m+N,l} = -\langle \mathbf{f}_m(\mathbf{r}), \mathcal{K}_0\{\mathbf{f}_l(\mathbf{r})\} + \mathcal{K}_1\{\mathbf{f}_l(\mathbf{r})\} \rangle,$$

$$\mathbf{Z}_{m,l+N} = -\mathbf{Z}_{m+N,l},$$

$$\mathbf{Z}_{m+N,l+N} = \left\langle \mathbf{f}_m(\mathbf{r}), \frac{\varepsilon_0}{\mu_0}\mathcal{L}_0\{\mathbf{f}_l(\mathbf{r})\} + \frac{\varepsilon_1}{\mu_1}\mathcal{L}_1\{\mathbf{f}_l(\mathbf{r})\} \right\rangle, m = 1, ..., N, l = 1, ..., N.$$

In Eqs. (12) and (13), the inner product is defined as $\langle \mathbf{f}_m(\mathbf{r}), \mathbf{Y}(\mathbf{r}) \rangle = \int_{S_m} \mathbf{f}_m(\mathbf{r}') \cdot \mathbf{Y}(\mathbf{r}') ds'$, where S_m is the support of the testing function $\mathbf{f}_m(\mathbf{r})$. The matrix system in Eq. (11) is solved for the unknown current coefficient vector $\mathbf{I}$. Once current coefficients are found, electric field can be computed by inserting Eq. (10) into Eq. (8). The loss probability can then be computed by putting the scattered electric field Eq. (6) into Eq. (4).

3. Numerical results

In this section, several examples are given to show the accuracy of the proposed solver. First, silver and gold spheres are simulated and compared with analytical results. Then, dimers composed of silver spheres or gold spheres are simulated to show the versatility of the proposed solver. Lastly, a dimer composed of a silver and a gold disk on a substrate is studied. In all of the examples, frequency-dependent relative permittivity of gold and silver is taken from Johnson–Christy experiments [16]. The outer medium is assumed to be free space.

3.1. Sphere

The first example is a silver sphere with a radius of 40 nm placed on the xy-plane such that the shortest distance to the electron beam, known as impact factor, is 10 nm [6]. The speed of the electron is $v = 0.5c$ corresponding to the energy of $E = 80$ keV. The sphere is meshed by triangular patches that have 241 nodes in total leading to 478 patches and 717 RWG basis functions. In BEM simulations, two different meshes are used. The first one is a triangular mesh composed of 625 nodes that gives almost three times denser mesh compared to FDSIE simulation. The other mesh has 1444 nodes which is the biggest mesh for a sphere available in the toolbox [6].

Loss probability is computed for different L and Δz values. Figure 1a shows the convergence of results for $\Delta z = 0.5$ nm and $L \in \{10, 20, 40, 60, 80, 100\}$ nm. Results converge around $L = 80$ nm for photon energies (light frequency) above 2eV. However, for lower frequencies, the path length L should be increased. This result indicates that the main contribution to the integral for high frequencies in Eq. (3) comes from the fields close to the NP. For lower frequencies, results converge around $L = 400$ nm. Note that this observation cannot be achieved by using the method in [6], which converts the line integral in Eq. (3) into a surface integral. Figure 1b shows the convergence of results for $\Delta z \in \{0.5, 1, 2, 4, 8\}$ nm and $L = 400$ nm. Results converge around $\Delta z = 1$ nm.
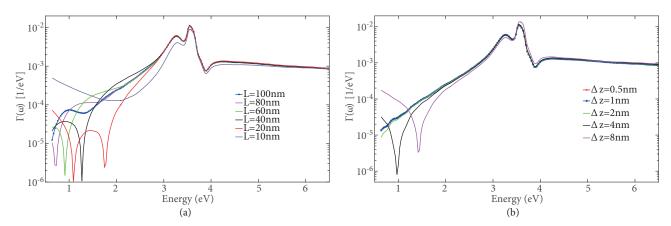
Figure 1. Convergence of EELS results as L changes (a). Convergence of results as Δz changes (b).
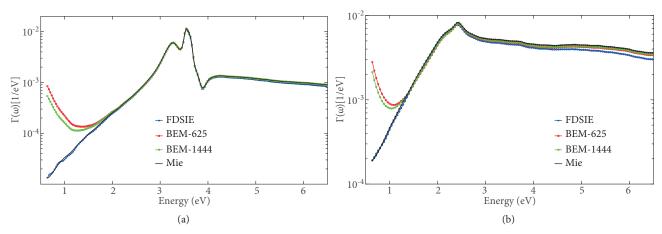

Figure 2. Comparison of FDSIE, BEM (625 and 1444 nodes), and analytical solver for the silver sphere (a) and the gold sphere (b).

Figure 2a depicts the comparison of FDSIE, BEM [6], and the analytical solver [6, 12] for the same silver sphere as in the previous case. Numerical results of FDSIE and BEM match reasonably well with analytical results, but results of BEM solver deteriorate below 1.7 eV even with a much denser (1444 nodes) mesh. Figure 2b shows the same kind of comparison for a gold sphere of radius 80 nm with an impact parameter of 2 nm [8]. Energy of the electron is 200 keV which corresponds to $v = 0.695c$. In this example, $L = 300$ nm and $\Delta z = 0.1$ nm used. Both solvers capture the general plasmonic behavior in comparison to the analytical solver. However, again, FDSIE provides closer EELS spectra to the analytical solver than the BEM solver for lower frequencies. One reason for this mismatch would be that the real part of the relative permittivity of gold and silver [16] reaches –60 at low frequencies. Hence, the simple collocation method used in [6] may not be sufficient to solve the problem at low frequencies and diverges. Another cause might be that BEM [6] suffers from low-frequency breakdown [17], yet a detailed analysis is beyond the scope of this work.

3.2. Dimer
In the next example, a dimer composed of two spheres on the xy-plane is analyzed. Radius of both spheres is 80 nm and the distance between them is 5 nm along the x-axis. Each sphere has 276 nodes, 548 patches, and 822 RWG in FDSIE simulations. In BEM, each sphere has 1444 nodes. The electron beam passes through the
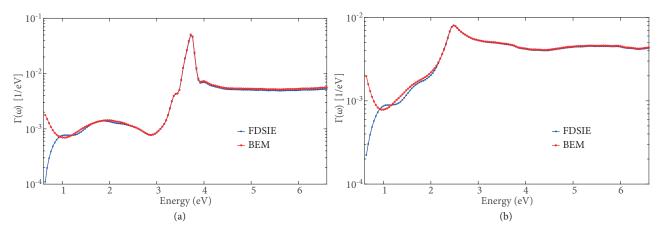
Figure 3. Comparison of FDSIE and BEM for the silver dimer (a) and the gold dimer (b).

midpoint between the spheres. The speed of the electron is $v = 0.5c$ corresponding to the energy of $E = 80$ keV. In that example, $L = 100$ nm and $\Delta z = 0.1$ nm. Figure 3a gives the comparison between FDSIE and BEM solvers for the silver dimer. Both results match with each other above 1 eV. In Figure 3b, the same comparison is given for the gold dimer. EELS spectra computed by FDSIE and BEM compare well above 1 eV, yet BEM produces higher values for low frequencies.

As the last example, a dimer composed of a silver disc and a gold disc on a substrate is considered. Each disc has a radius of 50 nm and a height of 30 nm. Substrate is chosen as rectangular prism with edge length of 300 nm along x- and y-axis and 50 nm along the z-axis. Discs are placed on the substrate (xy-plane) along the x-axis at a distance of 10 nm to each other. The mesh has total of 4642 triangular patches. The electron beam passes in the midpoint of the gap along the z-axis. The speed of the electron is $v = 0.765c$ corresponding to the energy of $E = 300$ keV. To calculate the energy loss, $L = 200$ nm and $\Delta z = 0.5$ nm used. This system has been studied experimentally on SiN substrate [18] and the relative permittivity is set to 4 for the substrate. Figure 4 shows the comparison between the FDSIE solution and the experimental results [18]. FDSIE solution matches the plasmonic resonance seen at 2.14 eV in the experiment. EELS computed by FDSIE solver captures the main shape of the experimental data. However, there are differences in the results. The main reason for these differences could be that in the simulations, perfect discs are used but in the experiments real NPs would have defects in their shapes.
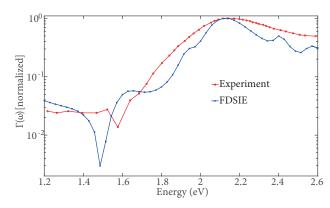

Figure 4. Comparison of FDSIE with an experiment of gold and silver discs on SiN substrate.

4. Conclusions

In this work, a PMCHWT–FDSIE solver was adapted for the simulation of EELS experiments for plasmonic gold and silver nanoparticles. The incident electromagnetic wave was created by swift electrons instead of conventional light sources. The back-scattered light from nanoparticles acted back to the swift electrons reducing their energy. The energy loss probability of electrons was computed by the proposed solver and compared with analytical and BEM solvers. Good agreement was shown with analytical solver even at low frequencies. Comparison with an experimental result showed a decent match, especially for the main plasmon resonance. The present work will be adapted for a time domain surface integral equation solver [19, 20].

Acknowledgment

References

[1] Aberasturi DJ, Serrano-Montes AB, Liz-Marzan LM. Modern applications of plasmonic nanoparticles: from energy to health. Adv Opt Mater 2015; 3: 602-617.

[2] Garcia de Abajo FJ. Optical excitations in electron microscopy. Rev Mod Phys 2010; 82: 209-275.

[3] Egerton RF. Electron energy-loss spectroscopy in the TEM. Rep Prog Phys 2009; 72: 1-25.

[4] Chu MW, Myroshnychenko V, Chen CH, Deng JP, Mou CY, Garcia de Abajo FJ. Probing bright and dark surface-plasmon modes in individual and coupled noble metal nanoparticles using an electron beam. Nano Lett 2009; 9: 399-404.

[5] Garcia de Abajo FJ, Howie A. Retarded field calculation of electron energy loss in inhomogeneous dielectrics. Phys Rev B 2002; 65: 1-17.

[6] Hohenester U. Simulating electron energy loss spectroscopy with the MNPBEM toolbox. Computer Physics Communications 2014; 185: 1177-1187.

[7] Bernasconi GD, Butet J, Flauraud V, Alexander D, Brugger J, Martin OJF. Where does energy go in electron energy loss spectroscopy of nanostructures? ACS Photonics 2017; 4: 156-164.

[8] Cao Y, Manjavacas A, Large N, Nordlander P. Electron energy-loss spectroscopy calculation in finite-difference time-domain package. ACS Photonics 2015; 2: 369-375.

[9] Bigelow NW, Vaschillo A, Iberi V, Camden JP, Masiello DJ. Characterization of the electron and photon driven plasmonic excitations of metal nanorods. ACS Nano 2012; 6: 7497-7504.

[10] Hoffmann J, Hafnera C, Leidenbergera P, Hesselbartha J, Burger S. Comparison of electromagnetic field solvers for the 3D analysis of plasmonic nano antennas. In: Proceedings of SPIE 7390 Europe Optical Metrology II; 2009; Munich, Germany. pp. 1-11.

[11] Rao S, Wilton D, Glisson A. Electromagnetic scattering by surfaces of arbitrary shape. IEEE Trans Antennas Propag 1982; 30: 409-418.

[12] Garcia de Abajo FJ. Relativistic energy loss and induced photon emission in the interaction of a dielectric sphere with an external electron beam. Phys Rev B 1999; 59: 3095.

[13] Medgyesi-Mitschang LN, Putnam JM, Gedera MB. Generalized method of moments for three-dimensional penetrable scatterers. J Opt Soc Am A 1994; 11: 1383-1398.

[14] Araujo M, Taboada J, Sols D, Rivero J, Landesa L, Obelleiro F. Comparison of surface integral equation formulations for electromagnetic analysis of plasmonic nanoscatterers. Opt Express 2012; 20: 9161-9171.

[15] Yla-Oijala P, Taskinen M, Sarvas J. Surface integral equation method for general composite metallic and dielectric structures with junctions. Prog Electromagn Res 2005; 52: 81-108.

[16] Johnson PB, Christy RW. Optical constants of the noble metals. Phys Rev B 1972; 6: 4370-4377.

[17] Zhu J, Omar S, Jiao D. Solution of the electric field integral equation when it breaks down. IEEE Trans Antennas Propag 2014; 62: 4122-4134.

[18] Flauraud V, Bernasconi GD, Butet J, Alexander DTL, Martin OJF, Brugger J. Mode coupling in plasmonic heterodimers probed with electron energy loss spectroscopy. ACS Nano 2017; 11: 3485-3495.

[19] Uysal IE, Ülkü HA, Bağcı H. Transient analysis of electromagnetic wave interactions on plasmonic nanostructures using a surface integral equation solver. J Opt Soc Am A 2016; 33: 1747-1759.

[20] Uysal IE, Sayed SB, Ülkü HA, Bağcı H. Electron energy loss spectroscopy simulation for plasmonic nanoparticles using a time domain surface integral equation solver. In: 2018 IEEE International Symposium on Antennas and Propagation and USNC-URSI Radio Science Meeting; 8–13 July 2018; Boston, MA, USA: IEEE.